Experimental Flowfield Visualization of a High Alpha Wing at Mach 1.62

James L. Pittman*
NASA Langley Research Center, Hampton, Virginia

Experimental oil-flow and tuft patterns and vapor-screen flow-visualization data were obtained on a cambered wing model at Mach = 1.62 for an angle-of-attack range of 0–14 deg. These data were used as flow diagnostic tools along with surface-pressure and force data and full-potential theory calculations. A large separation bubble was found on the lower wing surface at low angle of attack. The high-angle-of-attack flowfield was characterized by a large attached-flow leading-edge expansion followed by a crossflow shock. At $\alpha = 14$ deg the crossflow shock apparently induced discrete regions of streamwise separated flow, which were clearly indicated in the vapor-screen and oil-flow photographs.

Introduction

THE next generation of tactical aircraft will emphasize supersonic persistence in its mission scenario. Improved levels of performance relative to current aircraft are required to cruise for long distances and to maneuver at supersonic speeds. The interest in supersonic maneuver is a recent one, since present-generation tactical aircraft only have a supersonic dash capability.

The supersonic maneuver problem can be approached from two different perspectives: one is to allow the flow to separate at the wing leading edge and form a well-defined vortex system and the other is to control the leading-edge flow so that the flow remains attached over the entire wing. Although the structure of these two flowfields is entirely different, the end goal is the same, i.e., efficient supersonic maneuver. The state-of-the-art in vortex flow aerodynamics was recently summarized in a conference.[1-3] The attached-flow maneuver concept, which is the approach taken for the cambered wing discussed herein, is described in Ref. 4 and 5.

The attached-flow maneuver concept utilizes camber and a rounded leading edge to reduce wing surface-pressure gradients at the wing leading edge. The pressure gradients on the leading edge are thereby controlled so that the flow does not separate at the leading edge. If properly controlled, the wing leading-edge flowfield can attain a significant expansion which will provide a large lifting increment and also a large leading-edge thrust increment because of the wing camber. The expanded upper-surface flowfield will then compress through a crossflow shock which must also be controlled to prevent shock-induced boundary-layer separation.

The flowfield of the attached-flow maneuver concept is nonlinear and consequently requires a CFD solver for design. The NCOREL full-potential solver[6,7] for supersonic flow was developed, in part, as a design tool for the attached-flow maneuver concept and additionally as an analysis tool for complex configurations.[8,9]

Experimental verification of the attached-flow maneuver concept was obtained in the NASA Langley Unitary Plan Wind Tunnel and is described in Ref. 10. The test article was a highly swept cambered wing which was instrumented to obtain surface-pressure data in addition to force and moment data. Comparisons of the experimental pressure data and the full-potential calculations revealed that the basic design goal of attached leeside flow at high angle of attack was achieved. However, surface oil-flow data of the upper surface at high angle of attack showed a complex flow pattern which could not be totally understood with inviscid theory. Additionally, a comparison of the drag results from the experiment and full-potential theory showed a discrepancy at low angle of attack which could not be explained with the available experimental data. Subsequently, a more detailed flow-visualization experiment was performed to provide further verification and explanation of the high-angle-of-attack flowfield and to provide insight into the error in the computed drag at low angle of attack.

The intent of the present paper is to analyze the experimental flowfield-visualization data and to correlate this data with experimental force and pressure data and full-potential results.

Test Article Description

Figure 1 shows a photograph of the test article installed in the NASA Langley Unitary Plan Wind Tunnel. The test parameters are $M = 1.58$, 1.62, 1.66, 1.70, and 2.00 at a Reynolds number per foot of 2×10^6. The angle-of-attack range was 0–14 deg at 0 deg sideslip. Transition strips were placed behind the wing leading edge to assure fully turbulent boundary-layer flow.

An isolated wing planform was chosen to verify the attached-flow maneuver concept. This approach allowed a large test article which in turn allowed very accurate tolerances on the wing leading edge. The isolated wing also removed body influence from the verification procedure. The test article was constructed of aluminum and instrumented to obtain surfaces pressures at four spanwise stations and force and moment data. The pressure tubing can be seen in Fig. 1. Pressure data were taken initially; the pressure tubing was then removed from the aft end of the model and force data were taken.

Aerodynamic Design

A modified arrow wing planform based on future advanced fighter requirements[11] was selected for the detailed aerodynamic design. The planform is shown in Fig. 2, where six

Received June 16, 1987.

*Aerospace Engineer, Fundamental Aerodynamics Branch, High-Speed Aerodynamics Division. Associate Fellow AIAA.

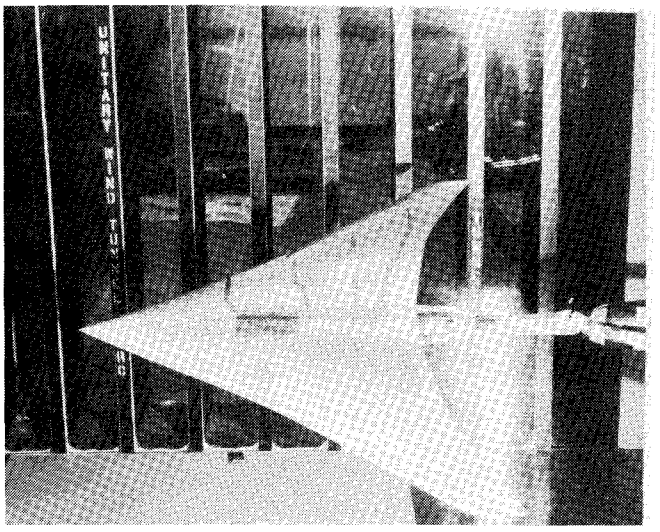

Fig. 1 Photograph of test article installed in NASA Langley Unitary Plan Wind Tunnel.

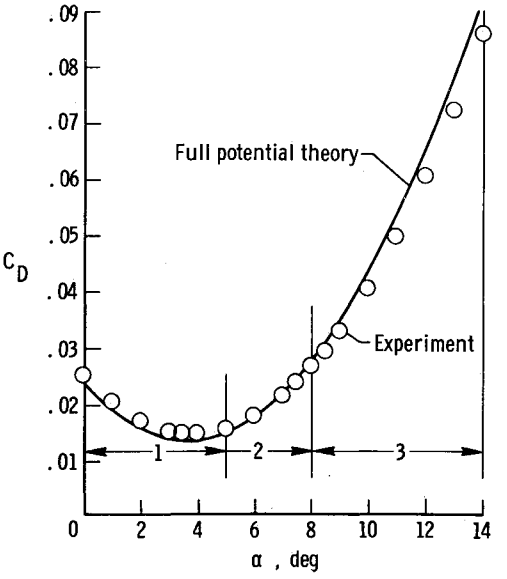

Fig. 3 Calculated and experimental drag coefficient plot at $M = 1.62$.

Station	X location	Pressure data	Vapor screen
1	10.6	Yes	Yes
2	15.5	Yes	Yes
3	19.9	Yes	Yes
4	24.4	Yes	Yes
5	27.0	No	Yes
6	28.0	No	Yes

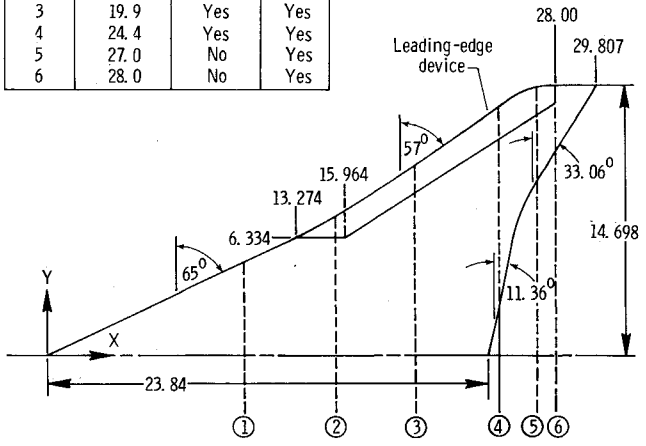

Fig. 2 Planform sketch of the cambered wing indicating the data stations.

spanwise data stations are indicated. Vaporscreen data were obtained at all six stations and pressure data were obtained at the first four. The wing sweep angle is initially 65 deg, fairing smoothly into a 57-deg sweep angle at about 40% semispan. The maximum thickness ratio of the wing is 4% at 40% of the local chord. The baseline thickness distribution is a NACA 0004-I4 type with a circular arc camber line. Local surface modifications were employed to control the leading-edge expansion and the strength of the crossflow shock. The details of the airfoil development are given in Ref. 10.

The design point is $M = 1.62$, $\alpha = 12$ deg, $C_L = 0.40$. This is considered to be a typical maneuver point for advanced tactical aircraft. At this design point a target pressure distribution was chosen that is characterized by a large leading-edge expansion, a relatively flat pressure plateau, and a recompression through a crossflow shock. The exact values of the nominal target pressure distribution were based on a parametric analysis from a modified linear-theory optimization method,[12] previous conical wing results,[13] empirical separation criteria,[14] and design experience. The actual design of the airfoil was obtained by iteration of the surface contours until the desired target pressure distribution was achieved. The key elements of the design process were an accurate full-potential solver, NCOREL,[6,7] and an analytic geometry description which could be easily modified for design work.

Analysis and Discussion

The experimental and computed drag coefficient of the isolated wing plotted vs angle of attack at $M = 1.62$ is shown in Fig. 3. The computed drag is obtained by summing the NCOREL result with a skin-friction calculation.[15] This skin-friction method is an empirical flat-plate method which assumes that the skin friction is invariant with angle of attack. At M = 1.62, 69 counts of skin-friction drag were added to the NCOREL result.

The drag coefficient plot is divided into three distinct regions. Region 1 is the low-angle-of-attack range where the full-potential theory underestimates the experimental drag. Region 2 is the mid-angle-of-attack range where the agreement is excellent and region 3 is the high-angle-of-attack range where the full-potential theory underestimates the drag coefficient. An analysis of the available surface-pressure data, a comparison of the experimental data and the full-potential results, and an analysis of the flow-visualization data are used to explain the flow in the three regions indicated in Fig. 3.

Region 2 is examined first, since this is the angle-of-attack range where the full-potential method provides the best estimate of the experimental data. An oil-flow and tuft pattern on the wing upper surface at $\alpha \approx 8$ deg is shown in Fig. 4. Due to the physical restrictions of the viewing area of the tunnel test section, the entire wing planform could not be photographed with a single camera. Consequently, two shots are necessary for each flow condition. The oil-flow and tuft patterns both indicate that smooth, attached flow exists on the wing at this condition except for two very small regions of flow separation at the wing tip trailing edges as indicated by the oil pattern. The two patches of oil accumulation near the wing tip trailing edge were noted to swirl during the experimental test. This swirling motion is consistent with the spiral node of separation as discussed by Peake and Tobak in Ref. 16. (The reader is referred to this reference for its large body of flow-visualization photographs along with supporting analysis and a definition of the topology of the flowfield.) The oil pattern also shows an oil accumulation line at the trailing edge. This oil accumulation line is a line of separation, since a trailing-edge shock exists at the trailing edge. The sharp turning of the oil-flow lines immediately ahead of the trailing edge on the inboard panel can be noted in Fig. 4. Striations in the

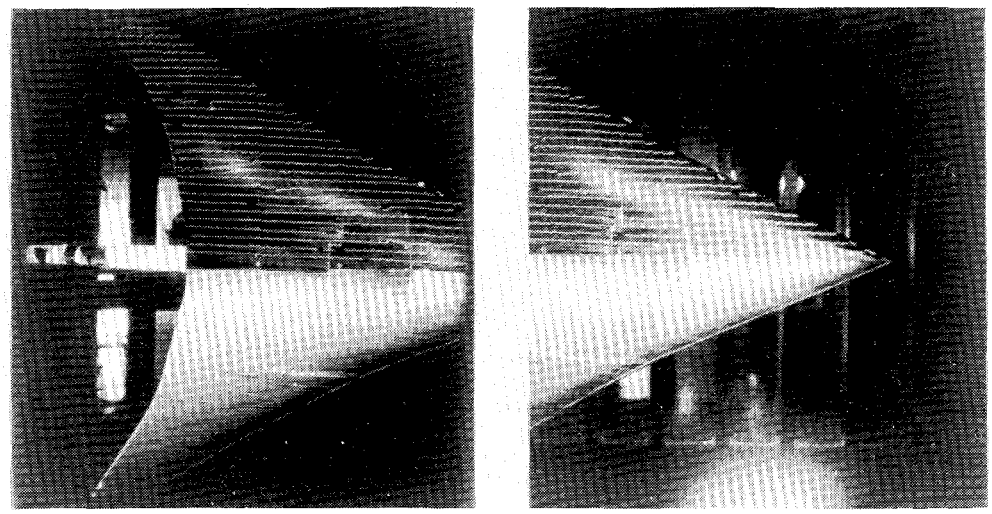

Fig. 4 Photograph of the wing upper surface oil-flow and tuft pattern at $\alpha \approx 8$ deg and $M = 1.62$.

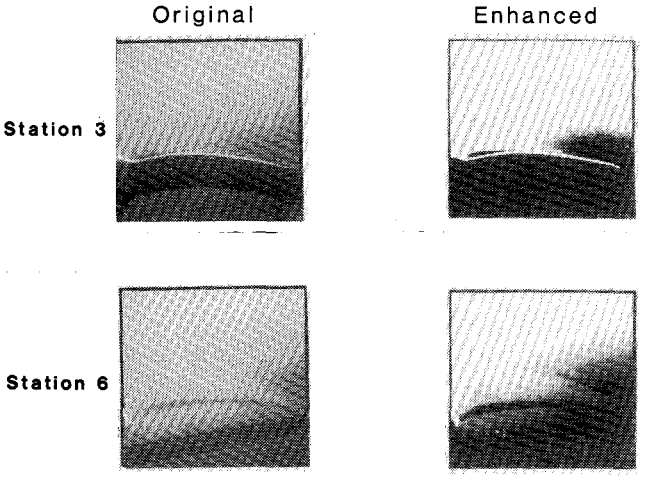

Fig. 5 Vapor screen photograph at stations 3 and 6, $\alpha = 8$ deg and $M = 1.62$.

oil-flow patterns are also evident near the wing centerline. These striations eminate from the interface of the balance cover plate with the rest of the model. The transition grit is clearly evident near the leading edge of the oil-flow wing panel.

The tuft pattern on the wing provides a clearer indication of the surface flow direction. The flow has an inboard flow component over most of the wing upper surface. A small portion of the wing has a nearly streamwise flow and the flow near the wing centerline has an outboard flow component which is largest near the trailing edge. Perhaps the most important benefit from the tufts is that tufts respond instantaneously to changes in the flow pattern whereas the oil, which must be highly viscous in order to remain on the wing during the tunnel startup process, responds very slowly. Consequently, the tufts can be used to determine when the oil flow has stabilized for a particular flow condition.

Vapor-screen photographs at two wing stations and $\alpha = 8$ deg are presented in Fig. 5. The first vapor-screen photograph is at station 3. This vapor screen shows that a relatively weak expansion occurs near the wing leading edge as indicated by the slightly darker area of the photograph. An enhanced image is shown next to the original. The gray scale of the original image had been significantly reduced in the enhanced image to emphasize the leading-edge expansion region. Overall, the flowfield is without regions of separated flow or strong crossflow shocks, which is consistent with the oil-flow and tuft patterns shown previously. The second vapor-screen photograph is from the wake region of the wing. This photograph clearly shows the trailing-edge shock and the shed-wing boundary layer which is curved because of the wing camber. These features are seen more clearly in the corresponding enhanced image. Also note that the shed wake is smooth, indicating the lack of large-scale disturbances in the boundary layer. The boundary layer thickens as it approaches the wing centerline; this is caused by the concavity of the wing upper surface near the balance housing.

A comparison of the full-potential surface-pressure calculations and the experimental data is shown in Fig. 6. Excellent agreement is noted over the entire wing surface, which is consistent with the drag result from Fig. 3. The full-potential theory indicates that the upper-surface flow expands to slightly supercritical crossflow Mach numbers behind the leading edge and then recompresses mildly.

The flowfield in the low-angle-of-attack range (region 1 of Fig. 3) is examined next. Intuitively, one would expect that the agreement between the full-potential theory and the experiment in this angle-of-attack range should be as good as the agreement noted in the mid-angle-of-attack range. However, this is clearly not the case. An examination of the oil-flow, tuft, and vapor-screen data on the wing upper surface in the low-angle-of-attack range ($\alpha \leq 6$ deg) revealed basically the same flow pattern as noted previously at $\alpha = 8$ deg (Figs. 4 and 5). Surface-pressure data were not obtained in the low-angle-of-attack range since the major focus of this effort was for high angle of attack.

The calculated results from the full-potential theory provide guidance as to the possible source of the disparity noted in the drag plot (Fig. 3). Information from the full-potential calculation at $\alpha = 0$ deg and a radial value of $R = 25.0$ in. behind the apex is presented in Fig. 7. The isobar pattern in this plane is shown on the left-hand side of the figure. The outer boundary is the computed position of the bow shock. The isobar pattern shows rapid changes in pressure on the lower surface of the wing. This is confirmed by the plot on the right-hand side of Fig. 7. The dotted line below the wing is the crossflow sonic line. Therefore, the crossflow inside this dotted line is supercritical. At high angle of attack, a supercritical crossflow region will develop on the upper surface. Therefore, due to the camber of the wing and the low angle of attack, the lower surface of the wing has become effectively the upper surface to the airflow.

The consequences of this flowfield can be assessed from the oil-flow and tuft patterns of the lower surface of the wing at $\alpha = 0$ deg (Fig. 8) The dominant feature of the oil-flow pattern is the dark line which extends aft along a ray from the apex.

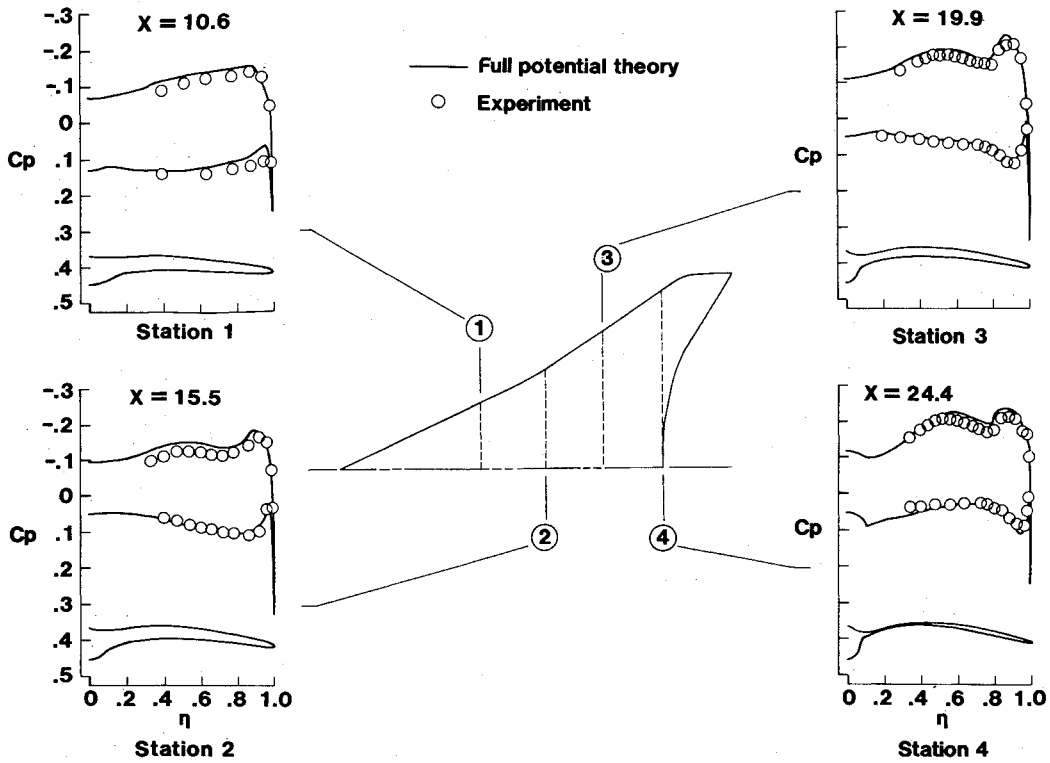

Fig. 6 Comparison of the full potential and experimental surface pressure data at four span stations at $\alpha = 7.92$ deg and $M = 1.62$.

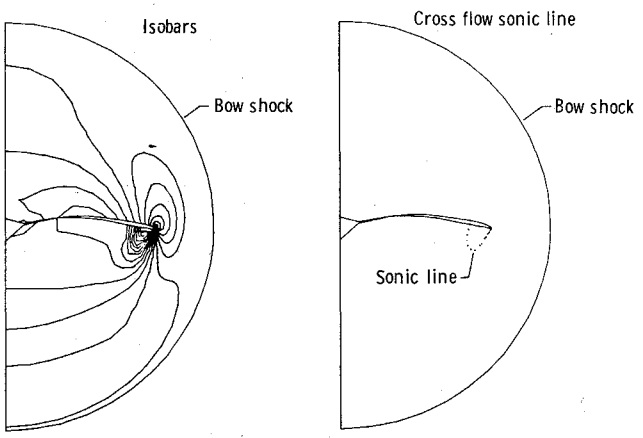

Fig. 7 Computed full-potential flowfield at $\alpha = 0$ deg, $R = 25.0$ in., and $M = 1.62$.

The oil on either side of this dark line flows in two different directions: streamwise flow for the region inboard of the dark line and leading-edge parallel flow for the region outboard of the dark line. This is shown more clearly by the tuft pattern, which also shows a distinct boundary with two different surface flow directions. In the oil-flow pattern note the absence of any flow striations, which were noted in the wing upper surface at $\alpha = 8$ deg (Fig. 4). This may indicate that the boundary layer does not have an array of discrete vortices embedded in it at $\alpha = 0$ deg. This occurrence was postulated in Ref. 16 as an explanation for a striated oil-flow pattern.

The vapor-screen photographs of the wing lower surface at $\alpha = 0$ deg in Fig. 9 show that a large separation bubble exists on the wing lower surface. The extent of the bubble corresponds to the dark line that was noted in the oil flow. Also note that the separation bubble is surrounded by a slightly expanded flowfield and that the boundary between the separation bubble and its surrounding flowfield is very distinct. A separation bubble can be differentiated from a vortex by considering the streamlines. A separation bubble is closed and contains streamlines which are entirely contained inside the bubble. Consequently, the bubble can be considered as a solid surface to the inviscid flow. A vortex, on the other hand, contains streamlines which originate from outside the vortex. These streamlines are said to be open. This separation bubble is therefore the likely source of the higher than predicted drag at low angle of attack.

The high-angle-of-attack flowfield is illustrated by the $\alpha = 14$ deg oil and tuft patterns in Fig. 10. The oil-flow pattern is characterized by a large number of distinct oil accumulation lines. The tuft pattern clearly shows several different regions of surface flow with inboard, outboard, and streamwise flow components. Large regions of the upper-surface tufts vibrated at high frequency during the test for these conditions, as indicated by the blurred tuft images on the film. These flow regions were extremely unsteady.

Some insight into the surface flow pattern can be gained from analyzing the vapor-screen photographs presented in Fig. 11. The vapor-screen data are presented at five wing stations. The first three stations are on the wing upper surface and the remaining two stations are in the wing wake region. The first photograph at station 2 clearly shows the leading-edge expansion region, which is abruptly terminated by a crossflow shock. There is also a distinct dark region just above the surface near the wing centerline. This region of separation may be related to the downward surface curvature that exists in the fairing region between the wing and the balance housing. The flowfield is delineated more clearly by the enhanced photograph which appears next to the original image. The gray scale on the enhanced image is reduced to obtain the maximum contrast. The enhanced image clearly shows the leading-edge expansion region, the crossflow shock which terminates as a step function, and the inboard separation region.

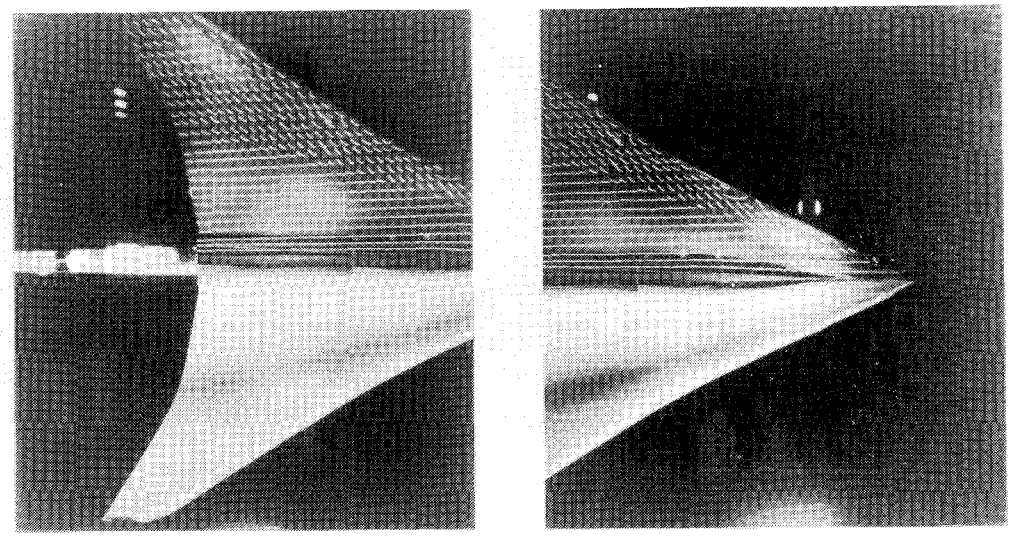

Aft portion Forward portion

Fig. 8 Photograph of the wing lower surface oil-flow and tuft pattern at $\alpha = 0$ deg, and $M = 1.62$.

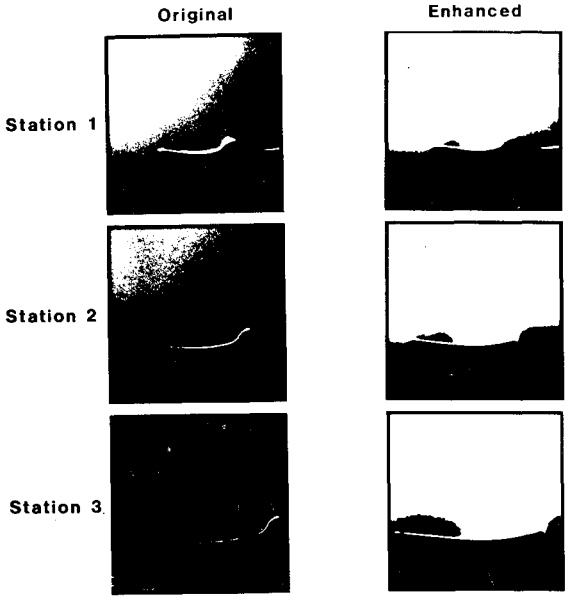

Fig. 9 Vapor-screen photographs on the wing lower surface at stations 1, 2, and 3, $\alpha = 0$ deg, $M = 1.62$.

The next vapor-screen image at station 3 indicates the same basic flow patterns with two additional dark regions in the boundary layer. The accompanying enhanced image shows that these regions of separation are distinct. It is possible that the crossflow shock is sufficiently strong to cause some boundary-layer separation at $\alpha = 14$ deg. The same flow pattern is noted in the vapor screen at station 4. It appears that there may be an additional region of boundary-layer separation at the foot of the crossflow shock but it is difficult to identify.

The next vapor screen at station 5 shows the complex flow pattern in the wing wake region. The shed boundary layer is a continuous dark region between the wing trailing edge at the right of the photograph and the sting on the left. The separation regions appear clearly but are merged in with the shed boundary layer. The trailing-edge shock is the sharp line above the shed wake. Note that the shape of the trailing-edge shock is influenced by the separation region in the boundary layer because the shock position is actually deflected upward by the boundary-layer separation region. The crossflow shock is still evident and sits atop the trailing-edge shock. The crossflow shock affects the shape of the trailing-edge shock, as can be noted by the discontinuity in the shock shape at the intersection point.

The final vapor-screen photograph is at station 6. The trailing-edge shock is farther above the shed boundary layer and consequently is less influenced by the separation regions, as indicated by the smoother shock shape. The intersection region of the crossflow and trailing-edge shocks is more clearly seen in the photograph. Similar vapor-screen photographs showing discrete separation regions above the boundary layer can be found in Fig. 180 of Ref. 16 and in Appendix B of Ref. 17.

The crossflow isobar pattern computed by the full-potential method at $R = 31.0$ in. is presented in Fig. 12. The accumulation of isobars around the wing leading edge indicates the large expansion in that area, and the nearly horizontal isobars in the wake region indicate the computed position of the trailing-edge shock. The crossflow sonic line is indicated by the dotted line on the right-hand side of the figure.

The flow-visualization and surface-pressure data can be used to give a better understanding of the vapor-screen flowfield. A tracing of the major oil accumulation lines from Fig. 10 is presented in Fig. 13, along with the airfoil shapes at the four pressure data stations and the experimental and the NCOREL surface-pressure data at the four stations. The tracings of the oil accumulation lines are identified by letters and the locations of these lines are indicated on the pressure plots and the airfoils. Also shown on the airfoils are the boundary-layer separation regions and the crossflow shock location measured from the vapor-screen photographs.

The first observation is that the NCOREL surface-pressure estimates agree well with the experimentally obtained data. The only significant disparity is at the crossflow shock. The full-potential theory correctly estimates the shock location but underestimates the strength of the shock. This error in surface pressure is maintained inboard of the crossflow shock and appears to be the reason for the overestimation of the drag coefficient in region 3 of Fig. 3. Since the full-potential theory predicts more negative pressure coefficients on a portion of the upper surface, a higher than measured lift and normal-force coefficient would result (see Fig. 11 of Ref. 10). The drag at high angle of attack is primarily due to the normal force; therefore, an overestimation of drag would be found.

The oil accumulation lines labeled A and D in Fig. 13 may be the same line. The break between these two lines occurs at the intersection of a leading-edge device with the wing and this intersection may cause the break between A and D. These two lines fall under the leading-edge pressure plateau region that exists between the leading edge and the crossflow shock and do not appear to be related to any distinct flow boundary.

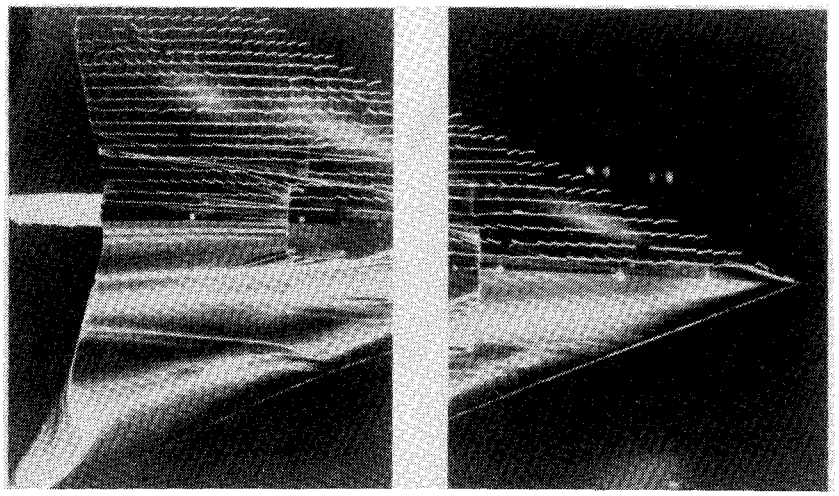

Aft portion Forward portion

Fig. 10 Photograph of the wing upper surface oil-flow and tuft pattern at $\alpha = 14$ deg and $M = 1.62$.

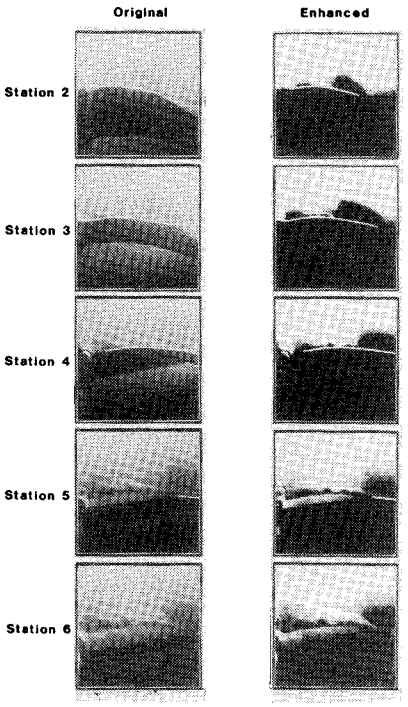

Fig. 11 Vapor-screen photographs on the wing upper surface at statons 2–6, $\alpha = 14$ deg, $M = 1.62$.

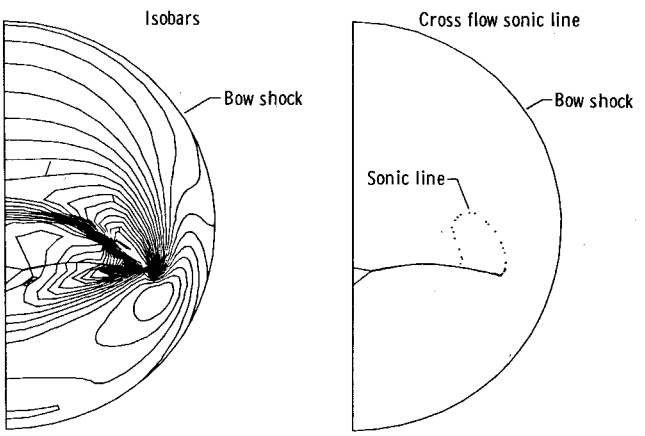

Fig. 12 Computed full-potential wake region flowfield at $R = 31.0$ in., $\alpha = 14$ deg, and $M = 1.62$.

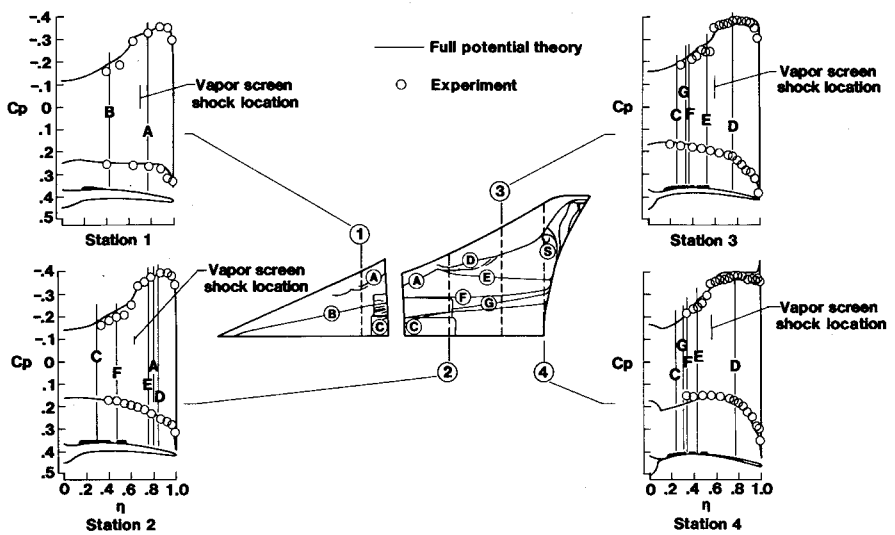

Fig. 13 Correlation of the flow visualization and surface pressure data at $\alpha = 14$ deg, $M = 1.62$.

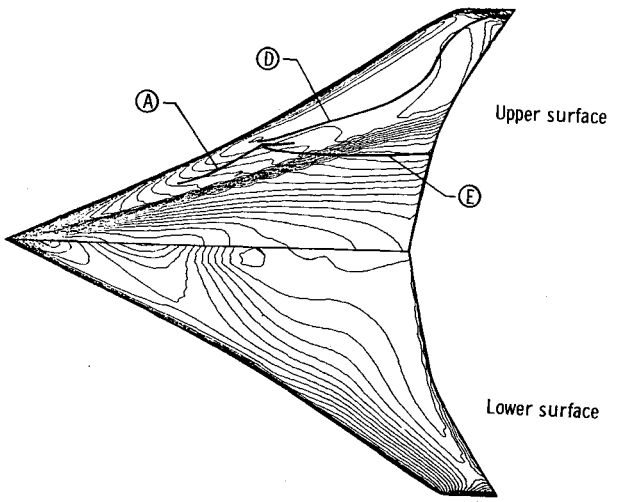

Fig. 14 Correlation of computed surface isobar patterns and experimental oil accumulation lines at $\alpha = 14$ deg, $M = 1.62$.

However, the location of these two lines does correspond to the point where the leading-edge pressure plateau begins a gradual compression. The oil accumulation lines E, F, and G correspond to the boundaries of the small separation regions that were noted on the vapor-screen photographs. Line C falls under the large separated region that fills the concave wing-balance housing fairing and therefore does not indicate a visible boundary. Line B, which is clearly visible on the fore portion of the wing, disappears into the numerous striations that originate at the interface between the balance cover plate and the wing. Lines F and G are the boundary lines of the striated region. A large spiral node of separation is identified as S in the figure. During the test, discrete drops of oil formed at the center of the spiral and jumped normal to the wing surface into the airflow at irregular intervals. A similar phenomenon is shown in Fig. 13 of Ref. 16 on a body of revolution.

The vapor-screen shock location that is indicated in Fig. 13 agrees well with the shock location, as indicated by the pressure data. However, none of the oil accumulation lines can be associated with the crossflow shock, which is an inviscid phenomenon. This can be seen more clearly in the computed surface isobar plot of Fig. 14. The computations are from the full-potential method, which correctly calculated the crossflow shock location as noted in Fig. 13. The accumulation of upper-surface isobars indicates the crossflow shock location. Superimposed on the isobar pattern is the location of several oil accumulation lines. The oil accumulation lines do not directly indicate the location of the crossflow shock.

Conclusion

Flow-visualization data were obtained on a cambered, isolated wing at $M = 1.62$ for an angle-of-attack range of 0–14 deg at 0 deg sideslip. Oil-flow and tuft patterns and vapor-screen data were used as flow diagnostic tools in conjunction with previously obtained force and surface-pressure experimental data and with full-potential calculations. A plot of the experimental and full-potential drag coefficient vs angle of attack was used to define three flow regions of interest: region 1, the low-angle-of-attack range where full-potential theory underestimates drag; region 2, the mid-angle-of-attack range where the agreement between experiment and full-potential theory is excellent; and region 3, the high-angle-of-attack range where full-potential theory overestimates the experimental drag.

The error in region 1 was traced to a large separation bubble that formed on the lower surface of the cambered wing at low angle of attack. The separation bubble was clearly indicated by the flow-visualization data. The full-potential theory indicated that the lower surface developed expansion flowfields in the crossflow plane under these conditions.

The excellent agreement between theory and experiment for region 2 was confirmed by a comparison of surface pressures from the full-potential theory and the experiment. The flow-visualization data indicated that the flowfield was correctly simulated by the full-potential model, i.e., one without significant rotational or viscous effects except for the boundary layer.

The error in the region 3 prediction was traced to an underestimation of the crossflow shock strength by the full-potential method. The vapor-screen data confirmed the existence of the desired high-angle-of-attack flow pattern, i.e., a large, attached flow expansion around the leading edge onto the upper surface followed by a relatively flat pressure plateau which is terminated by a crossflow shock. At the highest test $\alpha = 14$ deg, discrete regions of streamwise boundary-layer separation were noted immediately above the wing surface. These regions of separation may be shock-induced since they were not present at lower angles of attack. The boundaries of the regions of boundary-layer separation correlated with oil accumulation lines from the oil-flow test. Some of the oil accumulation lines fell under a region of streamwise separated flow or under the leading-edge expansion flowfield and therefore could not be related to a visible separation boundary. The vapor-screen method clearly indicated the crossflow shock, which did not correlate with any oil accumlation lines since the shock is an inviscid phenomenon.

References

[1] *Vortex Flow Aerodynamics*, Vol. I, NASA CP-2416, July 1986.

[2] *Vortex Flow Aerodynamics*, Vol. II, NASA CP-2417, July 1986.

[3] *Vortex Flow Aerodynamics*, Vol. III, NASA CP-2418, July 1986.

[4] Mason, W. H. and DaForno, G., "Opportunities for Supersonic Performance Gains Through Non-Linear Aerodynamics," AIAA Paper 79-1527, July 1979.

[5] Mason, W. H., "SC^3—A Wing Concept for Supersonic Maneuvering," AIAA Paper 83-1858, July 1983.

[6] Siclari, M. J., "The NCOREL Computer Program for 3D Nonlinear Supersonic Potential Flow Computations," NASA CR-3694, Aug. 1983.

[7] Siclari, M. J., "Supersonic Nonlinear Potential Flow Analysis—Interim Report," NASA CR-172456, Aug. 1984.

[8] Siclari, M. J., "Computations of Nonlinear Supersonic Potential Flow Over Three-Dimensional Surfaces," *Journal of Aircraft*, Vol. 20, May 1983, pp. 462–468.

[9] Siclari, M. J. and Pittman, J. L., "Application of NCOREL to Aircraft Configurations," AIAA Paper 86-1830, June 1986.

[10] Pittman, J. L., Miller, D. S., and Mason, W. H., "Supersonic, Nonlinear, Attached-Flow Wing Design for High Lift with Experimental Validation," NASA TP-2336, Aug. 1984.

[11] Bavitz, P. C., "The Impact of Technology and Combat Role in Advanced Fighter Concepts From Tactical Aircraft Research and Technology," NASA CP-2162, Part 2, Oct. 1980, pp. 857–875.

[12] Mason, W. H. and Rosen, B. S., "The COREL and W12SC3 Computer Programs for Supersonic Wing Design and Analysis," NASA CR-3676, Dec. 1983.

[13] Mason, W. H. and Miller, D. S., "Controlled Supercritical Crossflow on Supersonic Wings—An Experimental Validation," AIAA Paper 80-1421, July 1980.

[14] Kulfan, R. M. and Sigalla, A., "Real Flow Limitations in Supersonic Airplane Design," AIAA Paper 78-147, Jan. 1978.

[15] Sommer, S. C. and Short, B. J., "Free-Flight Measurements of Turbulent-Boundary-Layer Skin Friction in the Presence of Severe Aerodynamic Heating at Mach Numbers from 2.8 to 7.0," NACA TN-3391, March 1955.

[16] Peake, D. J. and Tobak, M., "Three-Dimensional Interactions and Vortical Flows with Emphasis on High Speeds," NASA TN-81169, March 1980.

[17] Miller, D. S. and Wood, R. M., "Lee-Side Flow Over Delta Wings at Supersonic Speeds," NASA TP-2430, June 1985.